ResearchGate

See discussions, stats, and author profiles for this publication at: https://www.researchgate.net/publication/262936119

In Situ Studies of the Temperature-Dependent Surface Structure and Chemistry of Single-Crystalline (001)-Oriented La0.8Sr0.2CoO3−δ Perovskite Thin Films

ARTICLE *in* JOURNAL OF PHYSICAL CHEMISTRY LETTERS · APRIL 2013

Impact Factor: 7.46 · DOI: 10.1021/jz400250t

CITATIONS
10

READS
59

9 AUTHORS, INCLUDING:

Dongkyu Lee
Massachusetts Institute of Technology
21 PUBLICATIONS **84** CITATIONS

SEE PROFILE

Michael D. Biegalski
Oak Ridge National Laboratory
129 PUBLICATIONS **2,495** CITATIONS

SEE PROFILE

Hua Zhou
Argonne National Laboratory
69 PUBLICATIONS **688** CITATIONS

SEE PROFILE

Hendrik Bluhm
Lawrence Berkeley National Laboratory
225 PUBLICATIONS **5,695** CITATIONS

SEE PROFILE

Available from: Zhenxing Feng
Retrieved on: 25 January 2016

THE JOURNAL OF PHYSICAL CHEMISTRY Letters

Letter

pubs.acs.org/JPCL

In Situ Studies of the Temperature-Dependent Surface Structure and Chemistry of Single-Crystalline (001)-Oriented $La_{0.8}Sr_{0.2}CoO_{3-\delta}$ Perovskite Thin Films

Zhenxing Feng,[†,‡] Ethan J. Crumlin,[†,‡,⊥] Wesley T. Hong,[†,§] Dongkyu Lee,[†,‡] Eva Mutoro,[†,‡,∇] Michael D. Biegalski,[∥] Hua Zhou,[◆] Hendrik Bluhm,[#] Hans M. Christen,[∥] and Yang Shao-Horn*[,†,‡,§]

[†]Electrochemical Energy Laboratory, [‡]Department of Mechanical Engineering, and [§]Department of Materials Science and Engineering, Massachusetts Institute of Technology, Cambridge, Massachusetts 02139, United States

[⊥]Adavenced Light Source and [#]Chemical Sciences Division, Lawrence Berkeley National Laboratory, Berkeley, California 94720, United States

[∇]BASF SE, Carl-Bosch-Strasse 3, 67056 Ludwigshafen, Germany

[∥]Center for Nanophase Materials Science, Oak Ridge National Laboratory, Oak Ridge, Tennessee 37831, United States

[◆]Advanced Photon Source, Argonne National Laboratory, Argonne, Illinois 60439, United States

Supporting Information

ABSTRACT: Perovskites are used to promote the kinetics of oxygen electrocatalysis in solid oxide fuel cells and oxygen permeation membranes. Little is known about the surface structure and chemistry of perovskites at high temperatures and partial oxygen pressures. Combining in situ X-ray reflectivity (XRR) and in situ ambient pressure X-ray photoelectron spectroscopy (APXPS), we report, for the first time, the evolution of the surface structure and chemistry of (001)-oriented perovskite $La_{0.8}Sr_{0.2}CoO_{3-\delta}$ (LSC_{113}) and $(La_{0.5}Sr_{0.5})_2CoO_{4+\delta}$ (LSC_{214})-decorated LSC_{113} ($LSC_{113/214}$) thin films as a function of temperature. Heating the (001)-oriented LSC_{113} surface leads to the formation of surface LSC_{214}-like particles, which is further confirmed by ex situ Auger electron spectroscopy (AES). In contrast, the $LSC_{113/214}$ surface, with activities much higher than that of LSC_{113}, is stable upon heating. Combined in situ XRR and APXPS measurements support that Sr enrichment may occur at the LSC_{113} and LSC_{214} interface, which can be responsible for its markedly enhanced activities.

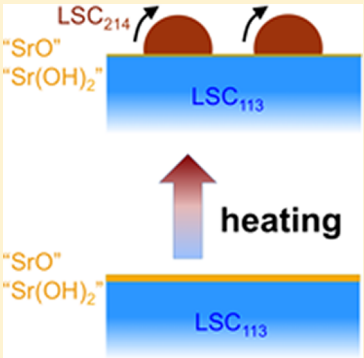

SECTION: Surfaces, Interfaces, Porous Materials, and Catalysis

Perovskites have been extensively explored as alternatives to expensive noble metals for oxygen electrocatalysis as they exhibit high activities not only in alkaline media ($O_2 + H_2O + 4e \leftrightarrow OH^-$)[1−5] but also in solid-state devices such as solid oxide fuel cells[6−13] and oxygen permeation membranes[14,15] at elevated temperatures ($O_2 \leftrightarrow O^{2-} + 2e$). Understanding the surface chemistry and electronic structure of single-crystal metal surfaces has led to the discovery of remarkably active surfaces for oxygen electrocatalysis, such as in platinum-based catalysts for proton exchange membrane fuel cells.[16−18] Recently, tuning single-crystalline perovskite surfaces has shown to greatly influence the activity for oxygen electrocatalysis ($O_2 + 4e^- \leftrightarrow 2O^{2-}$) at high temperatures.[10,12,13] In particular, up to 3 orders of magnitude in activity enhancement can be achieved by partially decorating the (001) surface of $La_{0.8}Sr_{0.2}CoO_{3-\delta}$ (LSC_{113}, a mixed electronic and ionic conducting perovskite)[8,19] with $(La_{0.5}Sr_{0.5})_2CoO_{4\pm\delta}$ (LSC_{214}).[10,20] However, little is known about how the oxide surface structures and chemistry changes from room temperature (RT), where the surfaces are characterized, to elevated temperatures, where the activities of oxygen electrocatalysis are measured.

In this study, we study the evolution in the surface structures of LSC_{113} and LSC_{214}-decorated LSC_{113} ($LSC_{113/214}$) thin films by using in situ X-ray reflectivity (XRR) as a function of temperature. By combining ex situ Auger electron spectroscopy (AES) with in situ ambient pressure X-ray photoelectron spectroscopy (APXPS), we correlate surface chemistry changes with the structural changes observed by XRR. These findings provide us unique insights into the surface structure and chemical stability of (001)-oriented LSC_{113} thin-film surfaces at high temperatures.

Epitaxial thin films of LSC_{113} were prepared by pulsed laser deposition (PLD) at 650 °C on yttria-stabilized zirconia (YSZ(001)) single crystals with gadolinium-doped ceria (GDC) as the buffer layer. $LSC_{113/214}$ films were fabricated by a subsequent deposition of LSC_{214} on a 15 000-pulse LSC_{113}

Received: February 3, 2013
Accepted: April 15, 2013
Published: April 15, 2013

 © 2013 American Chemical Society

film. Samples with 15 000 pulses (~90 nm) of LSC_{113} and $LSC_{113/214}$ samples (~90 nm $LSC_{113/214}$) with a 400-pulse LSC_{214} decoration (~4 nm LSC_{214}) were used for X-ray diffraction (XRD), electrochemical impedance spectroscopy (EIS), in situ XRR, in situ APXPS, and AES measurements. A similar prepared 90 nm LSC_{113} film with a 150-pulse LSC_{214} decoration (~1.5 nm, partially covered) was used for APXPS experiments. A 15 000-pulse (~160 nm) LSC_{214} film grown on GDC/YSZ(001) was used as the reference in AES experiments.

Normal and off-normal XRD patterns (Figure S1, Supporting Information (SI)) of as-deposited LSC_{113} and $LSC_{113/214}$ films revealed the following epitaxial relationships: $(001)_{pc}LSC_{113}//(001)_{cubic}GDC//(001)_{cubic}YSZ$ and $(100)_{pc}LSC_{113}//(110)_{cubic}GDC//(110)_{cubic}YSZ$ for out-of-plane and in-plane directions, respectively. The subscript "pc" denotes the pseudocubic notation, in which the rhombohedral structure of LSC_{113} bulk[21] is approximated as pseudocubic, as explained in our previous work.[12] The LSC_{214} decorations were too thin to be detected. Our previous studies[10,22] showed that thick LSC_{214} decorations have the following epitaxial relationships: $(001)_{tetragonal}LSC_{214}//(001)_{pc}LSC_{113}$ and $(100)_{tetragonal}LSC_{214}//(100)_{pc}LSC_{113}$ for out-of-plane and in-plane directions, respectively. Analysis of in situ XRD results performed at Advanced Photon Source (APS, shown in Table S1 and S2; details in the SI) shows that LSC_{113} films have slightly tensile strain in-plane (ε_{xx} = 0.87%) and compressive strain out-of-plane (ε_{zz} = −0.57%) at RT. As the temperature was increased from 220 to 350 °C, in-plane strains changed from tensile to compressive, while the out-of-plane strains changed from compressive to tensile, which is consistent with our previous study.[11]

In situ XRR measurements were performed to understand the surface and interface structural changes of LSC_{113} and $LSC_{113/214}$ thin films at elevated temperatures. Figure 1a shows in situ XRR experimental and fitted data of the 90 nm LSC_{113} sample at RT and 220, 350, and 400 °C under ambient air as a function of the modulus of the momentum transfer vector $Q = 4\pi \sin(2\theta/2)/\lambda$, where 2θ is the scattering angle and λ is the X-ray wavelength. The large, low-frequency oscillations are primarily related to the typical GDC layer thickness of ~5 nm, while the smaller, high-frequency oscillations can be attributed to the typical LSC_{113} film thickness of ~90 nm. The presence of oscillations extending to $Q > 0.9$ Å^{-1} indicates smooth, uniform film layers.

The XRR data of LSC_{113} were fitted by a four-layer model, which consisted of a semi-infinite YSZ crystal and four overlayers, an interfacial layer between the YSZ substrate and GDC, a GDC layer, a bulk LSC_{113} layer, and a surface LSC_{113} overlayer. The surface overlayer was separately modeled from the bulk LSC_{113} as our recent APXPS studies have revealed the presence of surface Sr-based secondary species on the (001)-oriented LSC_{113}.[11] The interfacial layer between the GDC layer and YSZ substrate was included to accurately describe the temperature dependence for the large oscillations associated with the GDC layer contribution. The inclusion of this interfacial layer is further justified by the facts that (1) there is a large lattice mismatch between GDC and YSZ (a_{YSZ} = 5.143 Å and a_{GDC} = 5.421 Å) and (2) the thermal expansion of GDC begins to deviate from that of YSZ at higher temperatures.[23,24] Similarly, a four-layer model is used for XRR fittings for $LSC_{113/214}$, but the top overlayer represents the LSC_{214} decoration, as shown in Figure 2. Three free parameters were allowed per layer, which included electron density, ρ,

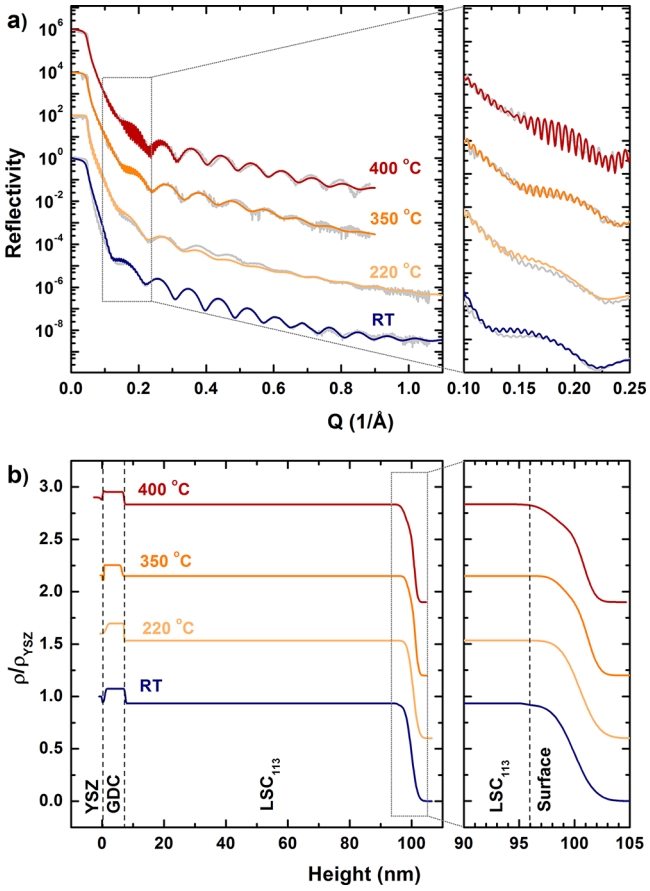

Figure 1. (a) In situ XRR data (silver) and fits (colored lines) of 90 nm LSC_{113}/GDC/YSZ at different temperatures (offset vertically for clarity): RT and 200, 350, and 400 °C in ambient air. The large, low-frequency oscillations are from GDC, while the inset shows the oscillations from LSC_{113}. (b) Electron density (EDY) depth profiles of the film at different temperatures obtained from XRR fit after being normalized to the bulk YSZ EDY. The corresponding parts from the model are presented. The inset shows the dramatic reduction of the surface EDY (see Table S3 (SI) for values). The sample was used for XRD, EIS, AES, and APXPS measurements.

RMS interface roughness in nm, σ, and the layer thickness in nm, t. In addition to these parameters, the roughness of the YSZ substrate was allowed to change while the bulk density was fixed, resulting in a total of 13 free parameters. The model fits are in excellent agreement with the data, with final χ^2 values no larger than 10 (Tables S3 and S4, SI).

Least-square fitting of the reflectivity data yielded the depth-dependent EDY profiles (eq S4, see the SI for details). Figure 1b shows the EDY of LSC_{113}/GDC/YSZ(001) at different temperatures. The RT profile shows a total film thickness of t_{tot} = 100 ± 1 nm, with an interfacial layer thickness of $t_{interface}$ = 0.9 ± 0.1 nm between GDC and the YSZ substrate, a GDC thickness of t_{GDC} = 6.6 ± 0.1 nm, a bulk LSC_{113} thickness of t_{LSC113} = 88.1 ± 0.4 nm, and a surface overlayer thickness of t_{top} = 4.4 ± 0.8 nm. The GDC thickness is consistent with our previous scanning transmission electron microscopy measurements on similarly prepared samples.[10] The LSC_{113} thickness (t_{LSC113} + t_{top}) is also in good agreement with our AFM measurements (94 nm), supporting the validity of our XRR models and fitting results. Interestingly, the EDY of $LSC_{113/214}$ obtained from XRR data fitting at RT reveals that the top layer is uniquely different from the layer underneath, which is not

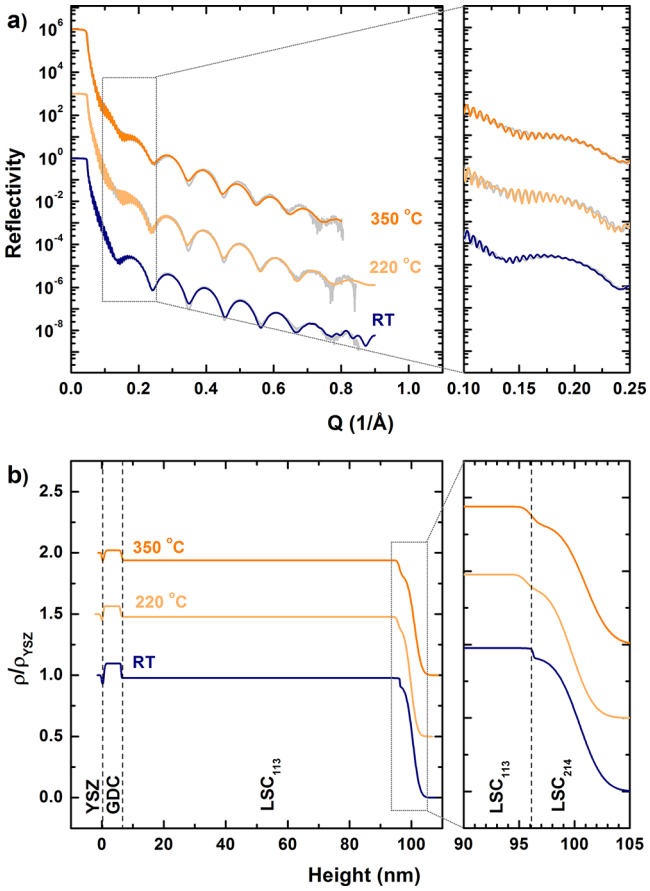

Figure 2. (a) In situ XRR data and fits of 4 nm LSC_{214}-decorated 90 nm LSC_{113}/GDC/YSZ at different temperatures: RT and 200 and 350 °C in ambient air. (b) The EDY obtained from the fits of the XRR data. The sample was used for XRD, EIS, and AES measurements.

noted for the EDY of LSC_{113}. The least-squares fitting of $LSC_{113/214}$/GDC/YSZ(001) at RT (Figure 2b) yields a total film thickness of t_{tot} = 100.4 ± 0.9 nm, with an interfacial layer thickness of $t_{interface}$ = 0.6 ± 0.4 nm between GDC and the YSZ substrate, a GDC thickness of t_{GDC} = 5.6 ± 0.2 nm, a LSC_{113} thickness of t_{LSC113} = 90.0 ± 0.1 nm, and an LSC_{214} thickness of t_{LSC214} = 4.2 ± 0.8 nm. The combined thickness of the LSC_{113} base film and the surface LSC_{214} overlayers is consistent with the AFM thickness measurement (94 nm), where detailed fitting results can be found in Tables S3 and S4 (SI).

Considerable changes were noted for the top overlayer of LSC_{113}/GDC/YSZ(001), while no significant changes in the bulk GDC or bulk LSC_{113} layer were found as the temperature was increased. The surface overlayer EDY was observed to reduce considerably and became more distinct from bulk LSC_{113} with increasing temperature, as shown in Figure 1b (details in Table S3 and Figure S6, SI). Such a reduction in EDY could result from particle formation on the surface upon heating. The proposed surface morphological changes are supported by AFM measurements (Figure S2, SI) before and after in situ XRR measurements, where the formation of particles and increased surface roughness were found. The fitting analysis results (Table S3, SI) also reveals a small increase beyond experimental uncertainty in the EDY for the interfacial layer between GDC and YSZ (corresponding to the change of the GDC oscillation amplitude in Figure 1a) but no detectable changes for the other parameters upon heating from RT to 220 °C. With further heating beyond 220 °C, no changes beyond experimental certainty were detected. This subtle increase in the EDY for the GDC/YSZ interface at 220 °C might be attributed to dissimilar strains in the interface associated with the abrupt structural change in the YSZ substrate from RT to 220 °C (Figure S4, SI). In contrast to LSC_{113}/GDC/YSZ(001), no significant changes were found for $LSC_{113/214}$ from RT to 350 °C (Figure 2a and Table S4, SI), indicating that the surface of $LSC_{113/214}$ is more stable than that of LSC_{113} upon heating. This result is in agreement with AFM measurements before and after in situ XRR studies, where minimal surface changes were observed (Figure S2, SI).

Previous work[10,25] has suggested that the interface between LSC_{113} and LSC_{214} might be responsible for markedly enhanced surface oxygen exchange kinetics of $LSC_{113/214}$. We further examined the interface by fitting $LSC_{113/214}$ XRR data using a five-layer model (Figure S5, SI), including an additional layer to account for the LSC_{113}/LSC_{214} interface. As compared to the four-layer model, the five-layer model adds only three fitting parameters but improves the detailed fitting of the LSC oscillations. Interestingly, as the temperature was increased, the EDY of the $LSC_{113/214}$ interface was reduced slightly relative to the LSC_{113} layer (see detailed parameters in Table S5, SI). It is unlikely that the reduced EDY at the interface within increasing temperature is a result of the strains between LSC_{113} and LSC_{214}, which have very close lattice constants (a_{LSC113} = 3.837 Å and a_{LSC214} = 3.802 Å), nor the different thermal expansions as the thermal expansion coefficient of LSC_{214} (14.3×10^{-6} K^{-1})[26] is very close to that of LSC_{113} (14.9×10^{-6} K^{-1}).[27] It is proposed that the reduced EDY at the interface can be attributed to increasing Sr concentration (with exchange of La from adjacent layers) at the interfacial region between LSC_{113} and LSC_{214}, which is in agreement with previous ab initio calculation results,[25] indicating strong Sr segregation tendencies at the LSC_{113}/LSC_{214} interface. Further experiments are needed to verify this hypothesis.

To spatially resolve the chemistry of surface particles formed upon heating on the LSC_{113} film, we performed ex situ AES measurements on the LSC_{113} and $LSC_{113/214}$ films before and after annealing at 550 °C for 6 h in pure oxygen flow, as shown in Figure 3a. No particles were found on the as-deposited LSC_{113} surface, which had a Sr/(La + Sr) ratio comparable to the nominal value (0.2). After annealing, discrete particles were noted on the LSC_{113} surface. AES data of the annealed LSC_{113} film show that the particles formed on the surface had higher Sr/(La + Sr) atomic ratios of ∼0.4 than the rest of the surface (∼0.1) and the as-deposited LSC_{113} surface (∼0.2), as shown in Figure S7 (SI). In addition, the Sr Auger spectral shape[28,29] of these surface particles was distinctly different from that of the rest of the annealed film surface and the as-deposited LSC_{113}. As the spectra of these surface particles resembles that of an as-deposited LSC_{214} (160 nm) sample prepared by PLD (details in the SI), it is postulated that the top surface of as-deposited LSC_{113} is not stable upon heating and decomposes to exhibit discrete LSC_{214}-like particles with higher stability at elevated temperatures. This hypothesis is further supported by the fact that the Auger analysis of the LSC_{214} surface (Figure S8, SI) showed minimal changes before and after annealing. Interestingly, the spectrum of particles from the as-deposited $LSC_{113/214}$ resembles that of the as-deposited LSC_{214} (Figure 3b), as expected from the LSC_{214} decoration. Minimal surface morphological change was found upon in situ XRR to 350 °C, indicative of greater surface stability than LSC_{113}. Upon

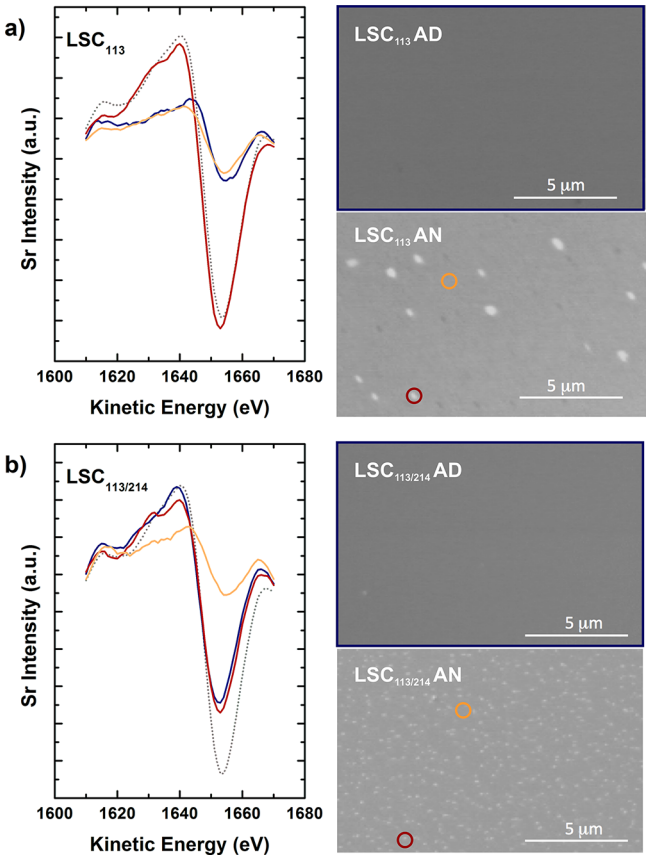

Figure 3. Sr Auger spectra (left) and scanning electron microscopy (SEM) images (right) for (a) 90 nm LSC_{113} and (b) 4 nm LSC_{214}-decorated 90 nm LSC_{113} ($LSC_{113/214}$) thin films. Auger data were collected from 10 × 10 μm^2 areas for as-deposited (AD) samples (blue) and from particles (dark red) and film surfaces (base film, yellow) of the same sample after annealing (AN) at 550 °C for 6 h in pure oxygen flow. The peak-to-peak values in Auger spectra reflect the Sr concentrations. These samples were also used for XRD, XRR, and EIS measurements. The 90 nm LSC_{113} was also used for APXPS. The dashed silver line is the Sr spectrum of a 160 nm LSC_{214} reference sample.

annealing at 550 °C, Auger analysis revealed that the LSC_{214} decoration became discrete LSC_{214}-like particles, whose density (4.25 particles/μm^2, 10% area coverage, estimated by averaging particles in three 5 × 5 μm^2 areas in SEM images) is much greater than that found for the annealed LSC_{113} surface (0.07 particles/μm^2, 1% area coverage). The thin-film LSC_{214} decorations are stable and do not reconstruct, as seen from XRR. Only after a very long time of annealing, the LSC_{214}-decorated films could be dewetted, but no chemical changes were found. On the basis of these, it is proposed that the formation of discrete LSC_{214}-like particles for LSC_{113} upon heating can be attributed to the following processes: (1) the top overlayer of the as-deposited LSC_{113} surface is decomposed to LSC_{214}-like and CoO_x particles (in contrast to LSC_{214}, CoO_x particles have been shown to reduce the ORR reaction activity[13]), and/or (2) surface secondary species on the surface of LSC_{113} react with LSC_{113} to form LSC_{214}-like particles, as shown in Figure 4. LSC_{214} is a layered perovskite, with excess AO planes between perovskite unit cells, and strontium-based Ruddlesden−Popper (A_2BO_4) phases have previously been synthesized by adding SrO between perovskite unit cells by PLD.[30] This decomposition has been reported in the bulk,[20,31−34] although at much higher temperatures and lower partial pressures of oxygen. The higher oxygen vacancies on the surface as reported in our previous work[11] may allow lower decomposition temperatures relative to that of the bulk. Adding LSC_{214} to the surface of LSC_{113} stabilizes the surface chemistry at elevated temperatures.

We then performed in situ APXPS measurements to examine the changes in the surface composition of LSC_{113} under thermal cycling. Figure 5a shows the XPS Sr spectra at 220, 370, and 520 °C at 1×10^{-3} atm of $p(O_2)$, where the surface is free of carbonate species.[11] The Sr 3d peak was found to exhibit three unique features, which could be fitted by two sets of Sr $3d_{5/2}$ and $3d_{3/2}$ doublets with an energy separation of ∼1.8 eV and a branching ratio of 1.5.[35,36] On the basis of our previous studies,[11,13,37] the low-energy component (∼132.2−132.7 eV) can be assigned to the near-surface region of the perovskite lattice, which is referred to as the "lattice" component, and the high-energy peak set (∼133.4−134.0 eV) can be associated with the perovskite surface termination and/or surface secondary phases such as $SrO/Sr(OH)_2$, which is referred as the "surface" component. Upon the first heating of the LSC_{113} film, the Sr 3d lattice component becomes much greater relative to the surface Sr component with increasing temperature, as shown in Figure 5b and c. This increase can be attributed to (1) the reactivity of surface secondary phases such as SrO with LSC_{113} to increase the Sr content in the perovskite structure and/or (2) the formation of surface LSC_{214}-like particles, which is supported by AES analysis discussed above. The later option is further supported by the fact that LSC_{214} was found to have similar Sr 3d features to LSC_{113} (∼132.4−132.6 eV, Figure S9 (SI)), the appearance of a distinct feature at higher binding energy of Co 3p with increasing temperature, suggesting the presence of Co in a lower oxidation state (Figure S10, SI), and the presence of CoO_x formed along with LSC_{214} during LSC_{113} decomposition.[20,31−34]

The transformed surface chemistry of LSC_{113} after the first heating was found to exhibit small changes in Sr upon subsequent thermal cycling (Figure 5b and d), indicating that the LSC_{113} surface with discrete LSC_{214}-like particles is stable at elevated temperatures. Interestingly, the Sr 3d lattice component was found to decrease by a small amount relative to the surface component with increasing temperature. This process was reversed upon cooling. The small increase in the surface Sr component can be attributed to the formation of SrO-related species, which is associated with increasing oxygen vacancies on the LSC_{113} surface with increasing temperature, as shown by recent DFT results.[11] The reversibility upon

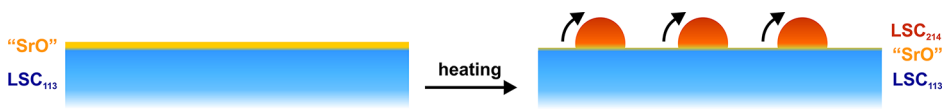

Figure 4. A schematic model to explain the different structural and chemical changes for LSC_{113}/GDC/YSZ thin-film SOFC cathode materials at RT (left) and high temperature (right). The surface LSC_{113} decomposes to LSC_{214} particles after heating.

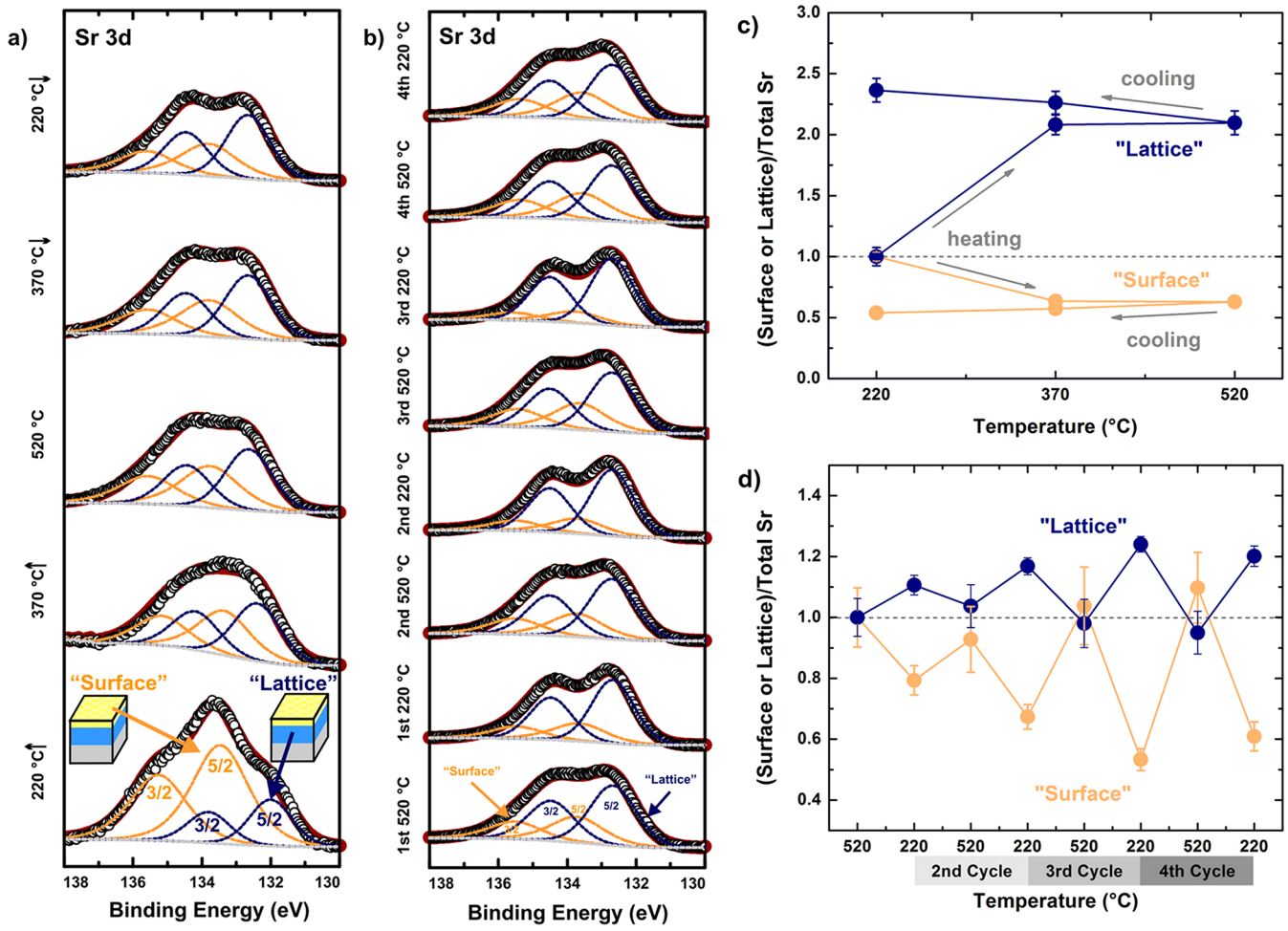

Figure 5. (a) Sr 3d XPS spectra of 90 nm LSC_{113} collected during the first heating. (b) Sr 3d XPS spectra of 90 nm LSC_{113} collected during subsequent temperature cycling at $p(O_2) = 1 \times 10^{-3}$ atm. (c) Sr 3d intensities of "lattice" and "surface" components of 90 nm LSC_{113} during the first heating, which was normalized to those obtained at 220 °C. (d) Sr 3d intensities of lattice and surface components of 90 nm LSC_{113} during subsequent temperature cycling, which was normalized to those obtained at 520 °C. The lattice component for the perovskite structure in the near-surface regions is shown in blue, while the surface component for surface secondary phases on the film is shown in orange. White circles are for the measured data, and gray dotted lines correspond to the background. The analysis of error bars can be obtained in the SI. Samples made in the same PLD experiment were also used for XRD, XRR, EIS, and AES measurements.

temperature cycling is similar to our recent in situ XPS studies under high vacuum (not near ambient pressure), which shows that the reversible surface Sr composition changes by applying an alternating cathodic and anodic bias.[37]

In summary, by combining both in situ hard (XRR) and soft (APXPS) synchrotron X-rays with ex situ Auger spectroscopy, we have observed different surface structural and chemical changes for (001)-oriented LSC_{113} and LSC_{214}-decorated LSC_{113} perovskite oxide thin films with increasing temperature. We find that the surface of the LSC_{113} perovskite structure is not stable, where the top several nanometers of LSC_{113} decompose to form surface LSC_{214}-like particles from 350 °C and above. In contrast, the LSC_{214}-decorated LSC_{113} perovskite structure is quite stable at high temperatures. In situ XRR data provide some evidence for Sr segregation at the LSC_{113} and LSC_{214} interface with increasing temperature, which could explain its activity enhancement relative to LSC_{113}. Understanding and tuning the surface structure and chemistry of perovskites at temperatures and partial oxygen pressures relevant to device operation is critical to identifying parameters that govern the activity and stability and developing highly active and stable catalysts for oxygen electrocatalysis.

■ EXPERIMENTAL METHODS

Materials. The 10 × 10 × 0.5 mm^3 (001)-oriented single crystals of 9.5 mol % Y_2O_3-stabilized ZrO_2 (YSZ) (Princeton Scientific, U.S.A., one sided polished) were used as substrates for thin-film deposition. PLD was utilized to first deposit a 20 mol % Gd-doped CeO_2 (GDC) film at 450 °C (~5 nm thick, estimated from scanning transmission electron microscopy on similarly prepared samples reported previously[10]). PLD was done under the following conditions: KrF excimer laser (λ = 248 nm), 10 Hz pulse rate, ~50 mJ pulse energy, and $p(O_2)$ = 50 mTorr. Additional details are provided in the SI.

Ex Situ XRD and Atomic Force Microscopy Characterization. XRD measurements were carried out on a four-circle diffractometer (PANalytical X'Pert) with Cu $K\alpha_1$ (λ = 1.5406 Å) radiation in normal and off-normal configurations.

A Veeco Nanoscope IV scanning probe microscope was used to obtain the surface morphology of as-deposited thin films after in situ XRR measurements and after annealing at 550 °C in 1 atm O_2 for 6 h (comparable to EIS experimental conditions). The film thicknesses were estimated by atomic force microscopy (AFM) measurements of patterned micro-

electrodes fabricated by photolithography for EIS measurements.

Electrochemical Impedance Spectroscopy (EIS). The surface exchange coefficients, k^q, of the LSC_{113} and $LSC_{113/214}$ films were determined by EIS measurements of microelectrodes (details in the SI). Enhanced ORR activity was found for heterostructured $LSC_{113/214}$ films compared to bare LSC_{113} (Figure S4, SI), in agreement with previous work.[10] The activity of $LSC_{113/214}$ films can change 1 to 2 orders of magnitude depending on the decoration coverage and partial pressure of oxygen. The measurements have previously shown that $LSC_{113/214}$ with partial coverage has the highest activity, while the thick LSC_{214} film decoration has the least enhanced activity compared to the bare LSC_{113} film.

In Situ XRR Characterization. In situ XRR measurements were performed at sector 33BM of the Advanced Photon Source (APS) in Argonne National Laboratory (ANL) using 20 keV X-rays with a beam size of 2.0 mm horizontally and 0.1 mm vertically and an incident flux of $\sim 10^{10}$ photons/s. Scattered X-rays were detected using a Cyberstar X1000 scintillation detector. Samples were placed on a custom-made heating stage and heated from RT up to 400 °C (the upper temperature of the heater used) under ambient air pressure. The heating rate was about 10 °C/min, and the temperature was held constant for about 20 min before collecting data at each temperature. Background-subtracted XRR data was analyzed using the Motofit[38] package in the IGOR Pro environment. Theoretical reflectivity curves were calculated using the Abeles matrix method and were fitted utilizing both Genetic optimization and Levenberg−Marquardt minimization algorithms. Additional details can be found in the SI.

Ex Situ AES Characterization. Both scanning electron microscopy (SEM) and AES measurements were conducted with a Physical Electronics 700 scanning Auger nanoprobe (PHI, U.S.A.) to analyze the surface chemistry change of the films. The films were annealed at 550 °C under 1 atm of $p(O_2)$ for 6 h and then air quenched to RT before AES data were collected. The AES data were collected from three different areas ($10 \times 10\ \mu m^2$) selected on the as-deposited samples and four points ($\sim 0.4 \times 0.4\ \mu m^2$, two for particles and two for the base film) on the annealed samples under ultrahigh vacuum conditions.

In Situ APXPS Characterization. Near-ambient pressure and high-temperature XPS data of the LSC_{113} and $LSC_{113/214}$ films were collected at Beamline 11.0.2 of the Advanced Light Source (ALS) in Lawrence Berkeley National Laboratory (LBNL). The thin-film samples were placed directly onto a ceramic heater, which was held in place by spring-loaded Au−Pd-coated tungsten tips. A thermocouple was mounted directly onto the sample surface for surface temperature measurements. A piece of Au foil was used for the binding energy (BE) calibration. All BEs were referenced to the La 4d at 101.2 eV. The spectra were collected in the following sequence (collection time of about 2 h per sequence): low-resolution survey (BE = −10−595 eV); high-resolution O 1s and Au 4f at a photon energy of 690 eV; and C 1s, La 4d, Sr 3d, Co 3p, and Au 4f at a photon energy of 390 eV. These spectra were collected at the following conditions: $p(O_2) = 1 \times 10^{-3}$ atm at $T = 25$ °C, $p(O_2) = 1 \times 10^{-3}$ atm at $T = 220$ °C, $p(O_2) = 1 \times 10^{-3}$ atm at $T = 370$ °C, and $p(O_2) = 1 \times 10^{-3}$ atm at $T = 520$ °C. The heating rate was about 10 °C/min, and the temperature was held constant for 20 min before beginning to collect data at each temperature. At temperatures above 220 °C under $p(O_2) = 1 \times 10^{-3}$ atm, carbonaceous species were removed from the surface (see the SI for details), allowing for cleaner deconvolution of the spectra free from surface carbonates. Only Sr 3d spectra are discussed. The Co 3p and La 4d are not discussed in detail because the complexity of the spectral features limits resolution of different chemical states. Details of XPS fitting parameters, peak positions, and assigned components can be found in Table S6 (SI). Details of XPS spectra can be found in Figures S10−S12 (SI).

■ ASSOCIATED CONTENT

Supporting Information

Details about sample preparation, EIS testing, XRD, AFM, AES, in situ XRR, and in situ APXPS characterizations. This material is available free of charge via the Internet at http://pubs.acs.org.

■ AUTHOR INFORMATION

Corresponding Author

*E-mail: shaohorn@mit.edu.

Notes

The authors declare no competing financial interest.

■ ACKNOWLEDGMENTS

This work was supported in part by the DOE (SISGR DESC0002633) and King Abdullah University of Science and Technology. The authors would like to thank the King Fahd University of Petroleum and Minerals in Dharam, Saudi Arabia, for funding the research reported in this paper through the Center for Clean Water and Clean Energy at MIT and KFUPM. The Advanced Photon Source and the Advanced Light Source are supported by the Director, Office of Science, Office of Basic Energy Sciences of the U.S. Department of Energy under Contracts DE-AC02-06CH11357 and DE-AC02-05CH11231, respectively. The PLD preparation performed was conducted at the Center for Nanophase Materials Sciences, which is sponsored at Oak Ridge National Laboratory by the Scientific User Facilities Division, Office of Basic Energy Sciences, U.S. Department of Energy.

■ REFERENCES

(1) Meadowcr, D. B. Low-Cost Oxygen Electrode Material. *Nature* **1970**, *226*, 847−848.

(2) Suntivich, J.; Gasteiger, H. A.; Yabuuchi, N.; et al. Design Principles for Oxygen-Reduction Activity on Perovskite Oxide Catalysts for Fuel Cells and Metal−Air Batteries. *Nat. Chem.* **2011**, *3*, 647−647.

(3) Suntivich, J.; Gasteiger, H. A.; Yabuuchi, N.; et al. Electrocatalytic Measurement Methodology of Oxide Catalysts Using a Thin-Film Rotating Disk Electrode. *J. Electrochem. Soc.* **2010**, *157*, B1263−B1268.

(4) Suntivich, J.; May, K. J.; Gasteiger, H. A.; et al. A Perovskite Oxide Optimized for Oxygen Evolution Catalysis from Molecular Orbital Principles. *Science* **2011**, *334*, 1383−1385.

(5) Savinell, R. F. Oxygen-Reduction Catalysts Picking Perovskites. *Nat. Chem.* **2011**, *3*, 501−502.

(6) Shao, Z. P.; Haile, S. M. A High-Performance Cathode for the Next Generation of Solid-Oxide Fuel Cells. *Nature* **2004**, *431*, 170−173.

(7) Kim, Y. M.; He, J.; Biegalski, M. D.; et al. Probing Oxygen Vacancy Concentration and Homogeneity in Solid-Oxide Fuel-Cell Cathode Materials on the Subunit-Cell Level. *Nat. Mater.* **2012**, *11*, 888−894.

(8) Adler, S. B. Factors Governing Oxygen Reduction in Solid Oxide Fuel Cell Cathodes. *Chem. Rev.* **2004**, *104*, 4791−4843.

(9) Chen, Y.; Jung, W.; Cai, Z. H.; et al. Impact of Sr Segregation on the Electronic Structure and Oxygen Reduction Activity of $SrTi_{1-x}Fe_xO_3$ surfaces. *Energy Environ. Sci.* **2012**, *5*, 7979−7988.
(10) Crumlin, E. J.; Mutoro, E.; Ahn, S. J.; et al. Oxygen Reduction Kinetics Enhancement on a Heterostructured Oxide Surface for Solid Oxide Fuel Cells. *J. Phys. Chem. Lett.* **2010**, *1*, 3149−3155.
(11) Crumlin, E. J.; Mutoro, E.; Liu, Z.; et al. Surface Strontium Enrichment on Highly Active Perovskites for Oxygen Electrocatalysis in Solid Oxide Fuel Cells. *Energy Environ. Sci.* **2012**, *5*, 6081−6088.
(12) la O', G. J.; Ahn, S. J.; Crumlin, E.; et al. Catalytic Activity Enhancement for Oxygen Reduction on Epitaxial Perovskite Thin Films for Solid-Oxide Fuel Cells. *Angew. Chem., Int. Ed.* **2010**, *49*, 5344−5347.
(13) Mutoro, E.; Crumlin, E. J.; Biegalski, M. D.; et al. Enhanced Oxygen Reduction Activity on Surface-Decorated Perovskite Thin Films for Solid Oxide Fuel Cells. *Energy Environ. Sci.* **2011**, *4*, 3689−3696.
(14) Wang, H. H.; Werth, S.; Schiestel, T.; et al. Perovskite Hollow-Fiber Membranes for the Production of Oxygen-Enriched Air. *Angew. Chem., Int. Ed.* **2005**, *44*, 6906−6909.
(15) Chen, C. S.; Feng, S. J.; Ran, S.; et al. Conversion of Methane to Syngas by a Membrane-Based Oxidation-Reforming Process. *Angew. Chem., Int. Ed.* **2003**, *42*, 5196−5198.
(16) Norskov, J. K.; Bligaard, T.; Rossmeisl, J.; et al. Towards the Computational Design of Solid Catalysts. *Nat. Chem.* **2009**, *1*, 37−46.
(17) Stamenkovic, V. R.; Fowler, B.; Mun, B. S.; et al. Improved Oxygen Reduction Activity on $Pt_3Ni(111)$ via Increased Surface Site Availability. *Science* **2007**, *315*, 493−497.
(18) Greeley, J.; Stephens, I. E. L.; Bondarenko, A. S.; et al. Alloys of Platinum and Early Transition Metals as Oxygen Reduction Electrocatalysts. *Nat. Chem.* **2009**, *1*, 552−556.
(19) Goodenough, J. B. Electronic and Ionic Transport Properties and Other Physical Aspects of Perovskites. *Rep. Prog. Phys.* **2004**, *67*, 1915−1993.
(20) Sase, M.; Yashiro, K.; Sato, K.; et al. Enhancement of Oxygen Exchange at the Hetero Interface of $(La,Sr)CoO_3/(La,Sr)_2CoO_4$ in Composite Ceramics. *Solid State Ionics* **2008**, *178*, 1843−1852.
(21) van Doorn, R. H. E.; Burggraaf, A. J. Structural Aspects of the Ionic Conductivity of $La_{1-x}Sr_xCoO_{3-\delta}$. *Solid State Ionics* **2000**, *128*, 65−78.
(22) Crumlin, E. J.; Ahn, S. J.; Lee, D.; et al. Oxygen Electrocatalysis on Epitaxial $La_{0.6}Sr_{0.4}CoO_{3-\delta}$ Perovskite Thin Films for Solid Oxide Fuel Cells. *J. Electrochem. Soc.* **2012**, *159*, F219−F225.
(23) Ishihara, T.; Kudo, T.; Matsuda, H.; et al. Doped $PrMNO_3$ Perovskite Oxide as a New Cathode of Solid Oxide Fuel-Cells for Low-Temperature Operation. *J. Electrochem. Soc.* **1995**, *142*, 1519−1524.
(24) Burmistrov, I.; Drozhzhin, O. A.; Istomin, S. Y.; et al. $Sr_{0.75}Y_{0.25}Co_{0.5}Mn_{0.5}O_{3-Y}$ Perovskite Cathode for Solid Oxide Fuel Cells. *J. Electrochem. Soc.* **2009**, *156*, B1212−B1217.
(25) Gadre, M. J.; Lee, Y. L.; Morgan, D. Cation Interdiffusion Model for Enhanced Oxygen Kinetics at Oxide Heterostructure Interfaces. *Phys. Chem. Chem. Phys.* **2012**, *14*, 2606−2616.
(26) Al Daroukh, M.; Vashook, V. V.; Ullmann, H.; et al. Oxides of the AMO_3 and A_2MO_4-Type: Structural Stability, Electrical Conductivity and Thermal Expansion. *Solid State Ionics* **2003**, *158*, 141−150.
(27) Chen, X. Y.; Yu, J. S.; Adler, S. B. Thermal and Chemical Expansion of Sr-Doped Lanthanum Cobalt Oxide ($La_{1-x}Sr_xCoO_{3-\delta}$). *Chem. Mater.* **2005**, *17*, 4537−4546.
(28) Chung, Y. W.; Weissbard, W. B. Surface Spectroscopy Studies of the $SrTiO_3$ (100) Surface and the Platinum−$SrTiO_3$ (100) Interface. *Phys. Rev. B* **1979**, *20*, 3456−3461.
(29) Zajac, G.; Zak, J.; Bader, S. D. Line-Shape Analyses of XVV Auger-Spectra of P(1 × 1)-$V_3Si(100)$ — Evidence for Autoionization Emission. *Phys. Rev. B* **1983**, *27*, 6649−6661.
(30) Palgrave, R. G.; Borisov, P.; Dyer, M. S.; et al. Artificial Construction of the Layered Ruddlesden-Popper Manganite $La_2Sr_2Mn_3O_{10}$ by Reflection High Energy Electron Diffraction Monitored Pulsed Laser Deposition. *J. Am. Chem. Soc.* **2012**, *134*, 7700−7714.
(31) Petrov, A. N.; Cherepanov, V. A.; Kononchuk, O. F.; et al. Oxygen Nonstoichiometry of $La_{1-x}Sr_xCoO_{3-\delta}$ ($0 < x \leq 0.6$). *J. Solid. State. Chem.* **1990**, *87*, 69−76.
(32) Seppänen, M.; Kytö, M.; Taskinen, P. Stability of the Ternary Phases in the La−Co−O System. *Scand. J. Metall.* **1979**, *8*, 199−204.
(33) Vashook, V. V.; Ullmann, H.; Olshevskaya, O. P.; et al. Composition and Electrical Conductivity of Some Cobaltates of the Type $La_{2-x}Sr_xCoO_{4.5-x/2\pm\delta}$. *Solid State Ionics* **2000**, *138*, 99−104.
(34) Morin, F.; Trudel, G.; Denos, Y. The Phase Stability of $La_{0.5}Sr_{0.5}CoO_{3-\delta}$. *Solid State Ionics* **1997**, *96*, 129−139.
(35) Vasquez, R. P. X-ray Photoelectron-Spectroscopy Study of Sr and Ba Compounds. *J. Electron Spectrosc.* **1991**, *56*, 217−240.
(36) van der Heide, P. A. W. Systematic X-ray Photoelectron Spectroscopic Study of $La_{1-x}Sr_x$-Based Perovskite-Type Oxides. *Surf. Interface Anal.* **2002**, *33*, 414−425.
(37) Mutoro, E.; Crumlin, E. J.; Pöpke, H.; et al. Reversible Compositional Control of Oxide Surfaces by Electrochemical Potentials. *J. Phys. Chem. Lett.* **2012**, *3*, 40−44.
(38) Nelson, A. Co-Refinement of Multiple-contrast Neutron/X-ray Reflectivity Data Using MOTOFIT. *J. App. Crystallogr.* **2006**, *39*, 273−276.